

## Article

# Power-Hardware-in-the-Loop for Stator Windings Asymmetry Fault Analysis in Direct-Drive PMSG-Based Wind Turbines<sup>†</sup>

Meysam Yousefzadeh<sup>1</sup>, Shahin Hedayati Kia<sup>2,\*</sup> , Mohammad Hoseintabar Marzebali<sup>3</sup>,  
Davood Arab Khaburi<sup>1</sup>  and Hubert Razik<sup>4</sup> 

<sup>1</sup> Center of Excellence for Power Systems Automation and Operation, Department of Electrical Engineering, Iran University of Science and Technology, Tehran 1311416846, Iran

<sup>2</sup> Laboratory MIS UR4290, University of Picardie “Jules Verne”, 33 rue St Leu, 80039 Amiens, France

<sup>3</sup> Department of Electrical Engineering and Robotic, Shahrood University of Technology, Shahrood 3619995161, Iran

<sup>4</sup> Laboratory Ampère UMR 5005, University of Lyon, 69622 Villeurbanne, France

\* Correspondence: shdkia@u-picardie.fr

† This paper is an extended version of our paper published in PEDSTC’2021.

**Abstract:** This article studies the stator windings asymmetry fault in direct-drive permanent magnet synchronous generator (PMSG)-based wind turbines (WTs), having passive converters at the generator side, through developing a power-hardware-in-the-loop (P-H-i-L) system. It is based on a digital real-time simulation (DRTS) of turbine blades, a wind generator in the *abc* reference frame, and a three-phase diode rectifier mathematical models. The DC voltage, provided by the model of the three-phase diode rectifier, is linked to a one-level hardware boost converter by using a programmable DC power supply. Furthermore, the maximum power point tracking technique, based on the optimal torque, is evaluated when the one-level boost converter supplies a resistive load. Stator windings asymmetry fault in the PMSG is identified by analyzing the rectifier output voltage, the rotor speed, and the electrical signatures of the boost converter. It shows that this kind of fault clearly gives rise to the amplitudes of both  $2 \cdot f_s$  and  $4 \cdot f_s$  frequency components in the mentioned signatures, where  $f_s$  is the main frequency component of the stator current. DRTSs are compared with digital offline simulations (DoSs), based on a Matlab/Simulink Simscape physical model, to demonstrate the efficacy of the proposed framework.

**Keywords:** emulation; hardware-in-the-loop; maximum power point tracking; permanent magnet synchronous generator; wind turbines; wind energy conversion systems



**Citation:** Yousefzadeh, M.; Hedayati Kia, S.; Hoseintabar Marzebali, M.; Arab Khaburi D.; Razik, H. Power-Hardware-in-the-Loop for Stator Windings Asymmetry Fault Analysis in Direct Drive PMSG-Based Wind Turbines. *Energies* **2022**, *15*, 6896. <https://doi.org/10.3390/en15196896>

Academic Editors: Abu-Siada Ahmed and Hasmat Malik

Received: 13 July 2022

Accepted: 15 September 2022

Published: 21 September 2022

**Publisher’s Note:** MDPI stays neutral with regard to jurisdictional claims in published maps and institutional affiliations.



**Copyright:** © 2022 by the authors. Licensee MDPI, Basel, Switzerland. This article is an open access article distributed under the terms and conditions of the Creative Commons Attribution (CC BY) license (<https://creativecommons.org/licenses/by/4.0/>).

## 1. Introduction

Online condition monitoring of wind energy conversion systems (WECSs) has attracted considerable research interest over the last decades. It is a crucial task for the reliability and availability improvement and maintenance cost minimization of such complex systems, which are composed of several mechanical and electrical components [1]. Rotor blades, main bearings, main low/high-speed shafts, and multistage gears are the main mechanical elements of the drive-train, while wind generators, power converters, and step-up power transformers are the main electrical components of WECSs [2]. Advanced real-time monitoring platforms aim to detect, localize and identify any defect in the WT system at an early stage by using data analysis and processing [3]. Prognosis deals with prediction of the remaining operating time before the faults result in failures, while resilient control refers to developing control laws that minimize the adverse influences of faults. It ensures that the system works normally even when it is faulty, and immediate replacement or repair is not necessary [4]. Moreover, the resilient control manages the performance degradation and avoids unexpected situations. An overview on fault diagnosis, prognosis and resilient control for WECSs has been well documented [4]. Newly developed

algorithms of online condition monitoring and fault-tolerant control can be evaluated at a lower cost by reproducing the real working condition of a WT using a reduced-scale experimental test rig [5]. Thanks to the rapid technological advancement of computers and field-programmable gate arrays (FPGAs), real-time platforms can currently incorporate parts of the system model [6,7]. Power systems, power electronics, and motor drives are fully simulated in real-time, initially using RTDS Technologies Inc. More recently, OPAL-RT Technologies Inc, open source real-time simulator DpSim, and LabVIEW FPGA are utilized for DRTS in model-in-the-loop (M-i-L), software-in-the-loop (S-i-L), and processor-in-the-loop (P-i-L) configurations [8–11]. Hardware-in-the-loop (H-i-L) is a kind of DRTS in which parts of the system are replaced by physical components. P-H-i-L is an H-i-L system in which a bidirectional power transfer between a hardware under test and a real-time digital simulator (RTDS) is performed [12]. Nowadays, P-H-i-L systems can significantly improve the DRTSs. Not only can it prevent the cumbersome task of real-time modeling of power converters at the device level [13,14], but also it offers a flexible test environment for the assessment of power converters and their related controllers [15]. P-H-i-L platforms have been widely utilized in diverse applications such as electric and hybrid electric vehicles, electric power plants and smart power grids, railway traction systems, and WECSs [15–20]. For instance, a fault-ride-through (FRT) capability test is realized by utilizing P-H-i-L facility in the certification process of up to 1 MW WECSs, based on IEC 61400 standard [21]. The torque of the missing rotor is realistically emulated on the main shaft of the system, and an advanced active damping control algorithm is elaborated to attenuate the vibrations in the drive-train [22]. To simulate the back-to-back converter in a 2 MW permanent magnet synchronous generator (PMSG)-based WECS in real-time, a signal level FPGA-based H-i-L system is designed with advanced refreshing rates of 4  $\mu$ s [23]. The proposed system evaluates electric control units (ECUs) in various working scenarios. The RT-lab DRTS platform is utilized for controller design and test in doubly-fed induction generator (DFIG)-based WTs [24]. In this regard, RT-Events and ARTEMIS, two Matlab/Simulink block sets, are specially designed to compensate for the problem of kHz-range PWM fixed-step simulation in inverter drives. In addition, a high-precision IGBT bridge model, called time-stamped bridge, is proposed to obtain accurate results in a 10  $\mu$ s to 50  $\mu$ s DRTS time-step range. The main objective was the rapid prototyping, testing, and validation of newly developed control techniques before their complete integration in full-scale WTs [24]. Recently, the concept of H-i-L has been proposed for the diagnosis of electrical and mechanical faults in induction machines [25–27]. However, they are limited to very simple setups where the electrical machine, coupled to a mechanical load, is studied in steady-state and transient conditions. Multiple open-circuit failures in the back-to-back converters of PMSG-based WTs are identified by the computation of instantaneous amplitude and current space vector using classical experimental test benches [28,29]. In these last works, the components of the drive-train, particularly the turbine blades, are not considered in the system, and the fault in PMSG is not studied.

This article presents a P-H-i-L framework for the real-time evaluation of newly developed condition monitoring and control techniques in direct-drive PMSG-based WECSs. It improves this evaluation significantly by integrating all drive-train components in the model. Moreover, the influence of stator windings asymmetry fault on PMSG-based WT variables, which is the main motivation of this work, will be investigated. The understudy configuration is composed of a PMSG, a three-phase diode rectifier, and a one-level boost converter, when this last one supplies a resistive load as depicted in Figure 1. Initially, the mathematical model of rotor blades with a constant pitch angle will be presented. Then, mathematical models of the PMSG in the *abc* reference frame and the one-level three-phase diode rectifier will be explained. Finally, these developed models will all be implemented in a real-time platform. The voltage obtained by the real-time model of three-phase diode rectifier is applied on a one-level hardware boost converter through a commercial programmable DC power supply. The maximum power point tracking (MPPT) technique, based upon the optimal torque, is evaluated where the one-level boost converter supplies a

resistive load. The proposed P-H-i-L framework introduces a reconfigurable DRTS environment that enables the analysis of stator windings asymmetry fault and its influence on the variables such as three-phase diode rectifier output voltage, rotor speed and electrical signatures of the boost converter. It avoids the installation of several sensors on classical reduced-scale test benches designed for the condition monitoring of WTs [5,30]. In addition, it will be demonstrated that the stator windings asymmetry fault clearly gives rise to the amplitudes of both  $2 \cdot f_s$  and  $4 \cdot f_s$  frequency components in the studied variables, where  $f_s$  is the main frequency component of the stator current. The efficacy of the proposed P-H-i-L framework and modeling approach is validated by comparing the DoS, which uses a variable-step ode23 solver and the elements of the SimPowerSystem in Matlab/Simulink software, with the DRTS results based on 12 kW PMSG WECS parameters. The real-time simulation environment allows studying other kinds of faults in the drive-train elements, such as shaft and turbine blades, along with the electrical elements, such as a three-phase diode rectifier for a wide power range of WTs. This can be carried out by developing realistic models of understudy components in both healthy and faulty working conditions. This leads to a lower cost rapid evaluation of advanced real-time condition monitoring approaches, based on the most sensitive signatures, which are commonly available in traditional experimental test benches by using high-cost instrumentation systems. In addition, fault-tolerant control methods can be designed to mitigate undesirable effects of faults in the energy generation.

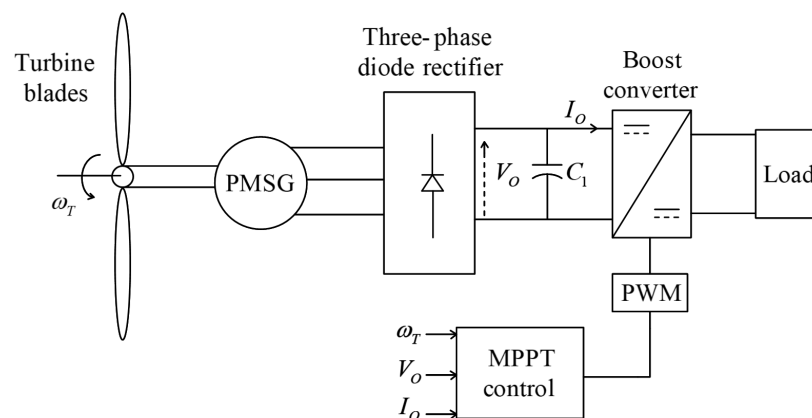


Figure 1. Simplified scheme of a direct-drive PMSG-based WT [7].

## 2. Modeling of a Direct-Drive PMSG-Based WT

Turbine blades, PMSG, and three-phase diode rectifier models, as shown in Figure 1, are described in this section. In this respect, the  $abc$  reference frame dynamic model of PMSG that facilitates the analysis of stator windings asymmetry fault is proposed.

### 2.1. Turbine Blades

The mechanical power extracted from the kinetic wind power is given by

$$P_T = 0.5 \cdot C_p \cdot \pi \cdot \rho \cdot r_T^2 \cdot v_w^3 \quad (1)$$

$C_p$  is defined as a function of TSR ( $\lambda$ ) [31]:

$$C_p(\lambda) = \lambda \cdot \left( C_{Tmax} - (\lambda - \lambda_{max})^2 \cdot K_T \right) \quad (2)$$

with

$$\lambda = \frac{\omega_T \cdot r_T}{v_w} \quad (3)$$

$C_{Tmax}$ ,  $\lambda_{max}$ , and  $K_T$  are constant terms in (2) that are defined based on the aerodynamic performance of turbine blades. The turbine torque can be written as

$$T_T = \frac{0.5}{\lambda} \cdot C_p(\lambda) \cdot \pi \cdot \rho \cdot v_w^2 \cdot r_T^3 \tag{4}$$

It has been depicted that  $\lambda^{OPT}$ , which is the optimal value of  $\lambda$ , is a constant term [32]. Thus, the optimal torque for direct-drive WT's can be obtained by

$$T_T^{OPT} = \frac{1}{2} \cdot \rho \cdot \pi \cdot r_T^5 \cdot \frac{C_p(\lambda^{OPT})}{\lambda^{OPT3}} \cdot \omega_T^2 = K^{OPT} \cdot \omega_T^2 \tag{5}$$

2.2. Wind Generator

Three-phase stator voltages of round rotor PMSG in the *abc* reference frame are given by (Figure 2) [2,33].

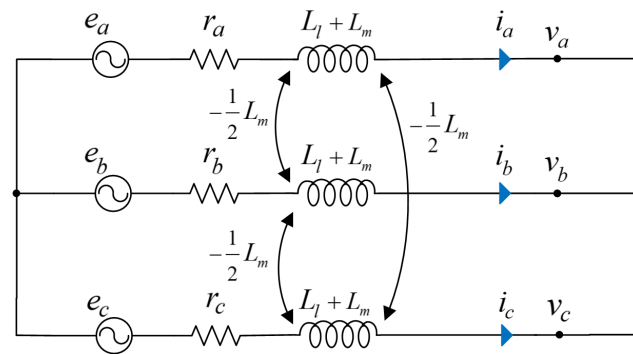


Figure 2. PMSG model in the *abc* reference frame [2,33].

$$\mathbf{V}_{abc} = -\mathbf{R}_{abc} \cdot \mathbf{i}_{abc} + \frac{d}{dt} \mathbf{\Psi}_{abc} \tag{6}$$

with

$$\mathbf{V}_{abc} = \begin{bmatrix} v_a \\ v_b \\ v_c \end{bmatrix}, \mathbf{R}_{abc} = \begin{bmatrix} r_a & 0 & 0 \\ 0 & r_b & 0 \\ 0 & 0 & r_c \end{bmatrix}, \mathbf{i}_{abc} = \begin{bmatrix} i_a \\ i_b \\ i_c \end{bmatrix} \tag{7}$$

$$\mathbf{\Psi}_{abc} = \begin{bmatrix} \phi_a \\ \phi_b \\ \phi_c \end{bmatrix} = - \begin{bmatrix} L_l + L_m & -\frac{L_m}{2} & -\frac{L_m}{2} \\ -\frac{L_m}{2} & L_l + L_m & -\frac{L_m}{2} \\ -\frac{L_m}{2} & -\frac{L_m}{2} & L_l + L_m \end{bmatrix} \cdot \begin{bmatrix} i_a \\ i_b \\ i_c \end{bmatrix} + \psi_r \cdot \begin{bmatrix} \cos(P_p \theta_T) \\ \cos(P_p \theta_T - \frac{2\pi}{3}) \\ \cos(P_p \theta_T + \frac{2\pi}{3}) \end{bmatrix} \tag{8}$$

To model the stator windings asymmetry fault correctly in PMSG, the stator line voltages need to be determined as

$$\begin{bmatrix} v_{ab} \\ v_{bc} \\ v_{ca} \end{bmatrix} = \begin{bmatrix} v_a - v_b \\ v_b - v_c \\ v_c - v_a \end{bmatrix} = - \begin{bmatrix} r_a & -r_b & 0 \\ 0 & r_b & -r_c \\ -r_a & 0 & r_c \end{bmatrix} \cdot \begin{bmatrix} i_a \\ i_b \\ i_c \end{bmatrix} + \frac{d}{dt} \begin{bmatrix} \phi_a - \phi_b \\ \phi_b - \phi_c \\ \phi_c - \phi_a \end{bmatrix} \tag{9}$$

with

$$\begin{bmatrix} \phi_a - \phi_b \\ \phi_b - \phi_c \\ \phi_c - \phi_a \end{bmatrix} = - \begin{bmatrix} L_l + \frac{3}{2}L_m & -L_l - \frac{3}{2}L_m & 0 \\ 0 & L_l + \frac{3}{2}L_m & -L_l - \frac{3}{2}L_m \\ -L_l - \frac{3}{2}L_m & 0 & L_l + \frac{3}{2}L_m \end{bmatrix} \cdot \begin{bmatrix} i_a \\ i_b \\ i_c \end{bmatrix} + \psi_r \cdot \begin{bmatrix} \cos(P_p \theta_T) - \cos(P_p \theta_T - \frac{2\pi}{3}) \\ \cos(P_p \theta_T - \frac{2\pi}{3}) - \cos(P_p \theta_T + \frac{2\pi}{3}) \\ \cos(P_p \theta_T + \frac{2\pi}{3}) - \cos(P_p \theta_T) \end{bmatrix} \tag{10}$$

The total input power can be written as

$$P_e = -(v_a i_a + v_b i_b + v_c i_c) = -[i_a \quad i_b \quad i_c] \cdot \begin{bmatrix} v_a \\ v_b \\ v_c \end{bmatrix} \tag{11}$$

Substituting (6) into (11), yields

$$P_e = (r_a i_a^2 + r_b i_b^2 + r_c i_c^2) + [i_a \quad i_b \quad i_c] \cdot \begin{bmatrix} L_l + L_m & -\frac{L_m}{2} & -\frac{L_m}{2} \\ -\frac{L_m}{2} & L_l + L_m & -\frac{L_m}{2} \\ -\frac{L_m}{2} & -\frac{L_m}{2} & L_l + L_m \end{bmatrix} \cdot \frac{d}{dt} \begin{bmatrix} i_a \\ i_b \\ i_c \end{bmatrix} - \psi_r \cdot [i_a \quad i_b \quad i_c] \cdot \frac{d}{dt} \begin{bmatrix} \cos(P_p \theta_T) \\ \cos(P_p \theta_T - \frac{2\pi}{3}) \\ \cos(P_p \theta_T + \frac{2\pi}{3}) \end{bmatrix} \tag{12}$$

It is well-known that only the third term in (12) produces the electromagnetic torque given by

$$T_e = \frac{P_m}{\omega_T} \tag{13}$$

which yields

$$T_e = P_p \cdot \psi_r \cdot \left[ \sin(P_p \theta_T) \cdot i_a + \sin(P_p \theta_T - \frac{2\pi}{3}) \cdot i_b + \sin(P_p \theta_T + \frac{2\pi}{3}) \cdot i_c \right] \tag{14}$$

The turbine rotor torque and speed for direct-drive WTs are related together by

$$T_T - T_e = J_t \cdot \frac{d}{dt} \omega_T + B_t \cdot \omega_T \tag{15}$$

The above relation is written to obtain a positive value of  $\omega_T$ .

### 2.3. Three-Phase Diode Rectifier

Figure 1 illustrates how three-phase diode rectifiers have been used in the generator-side power conversion of a WECS due to the unidirectional power flow. Typically, this component is modeled by using the commutation function approach when it is supplied by an ideal power grid. However, if imperfections such as line inductance and supply unbalance are considered, the previous model will give imprecise results [34]. In this article, the model of a three-phase diode rectifier is realized by considering all possible diodes' conduction  $P_i$  ( $i = 0, 1, 2, \dots, 6$ ) and overlapping  $O_j$  ( $j = 1, 2, \dots, 6$ ) stages depicted in Figure 3. The transition between  $P_i$  and  $O_j$  stages is carried out based on the algorithm shown in Figure 4 [34]. An ideal model is used for all diodes, i.e., the voltage across each one is zero ( $v_{d_j} = 0$ ) in on-state, and the current through is zero ( $i_{d_j} = 0$ ) in off-state. It should be noted that in all  $P_i$ , only two diodes are in on-state, whereas in all  $O_j$ , three diodes are in on-state. All diodes are in off-state in  $P_0$  (starting stage), and the voltages across diodes allow the identification of two conduction diodes in the next  $P_i$  ( $i > 0$ ). Furthermore, the transition between  $P_i$  and  $O_j$  needs the knowledge of the PMSG stator phase currents ( $i_a, i_b$  and  $i_c$ ) that can be obtained by using (9). In the previous expression, PMSG stator line voltages ( $v_{ab}, v_{bc}$  and  $v_{ca}$ ) need to be defined for each  $P_i$  and  $O_j$  stage. For instance, during  $P_1$ , both  $d_1$  and  $d_5$  are in on-state; hence, the stator line voltages and  $v_{d6}$  can be obtained by

$$v_{ab} = V_O \quad v_{bc} = e'_{bc} + \frac{1}{2}(e'_{ab} - V_O) \quad v_{ca} = e'_{ca} + \frac{1}{2}(e'_{ab} - V_O) \quad v_{d6} = \frac{1}{2}(e'_{ab} - V_O) + e'_{bc} \tag{16}$$

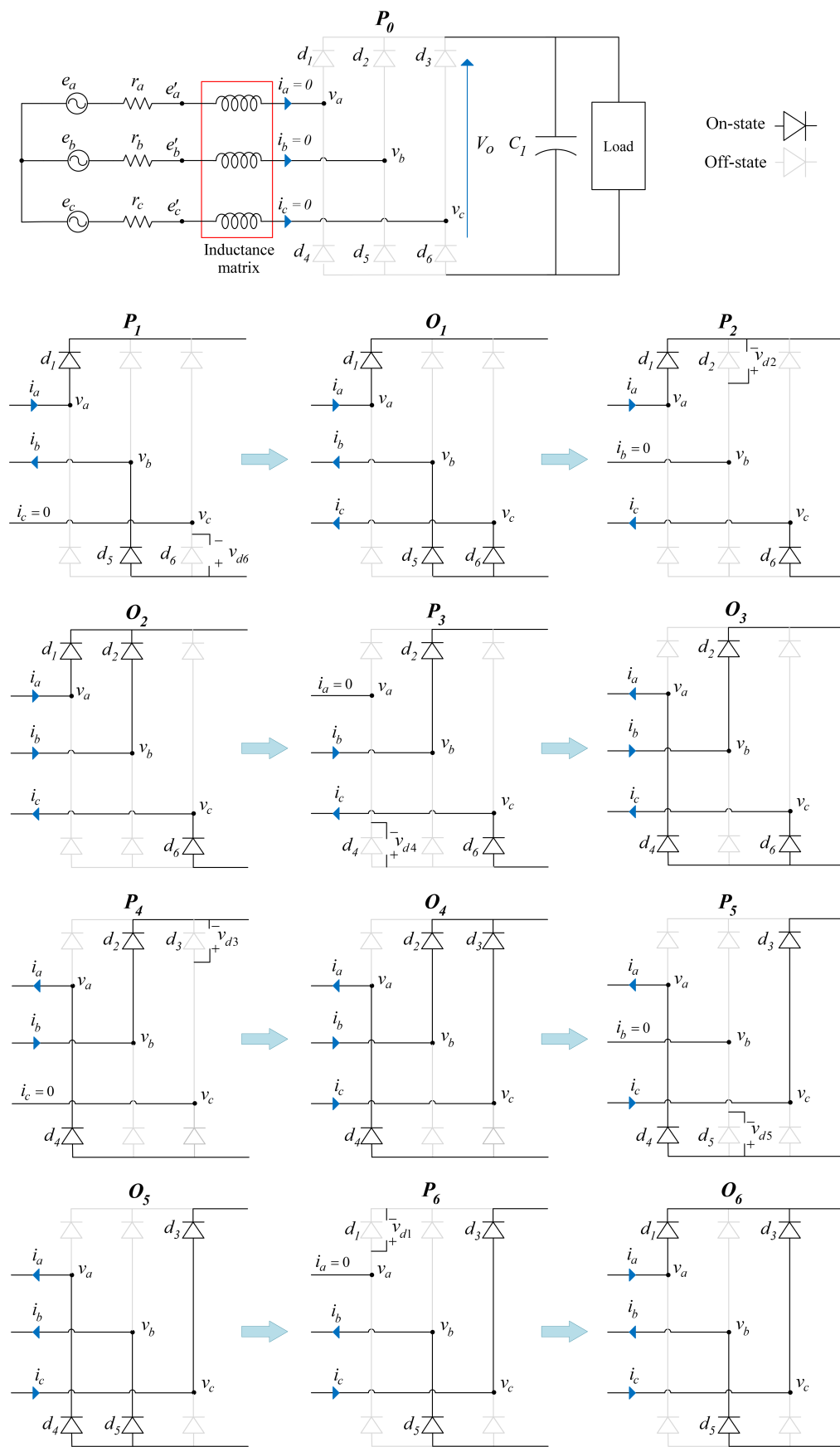


Figure 3. Three-phase diode rectifier model in conduction  $P_i$  and overlapping  $O_j$  stages.

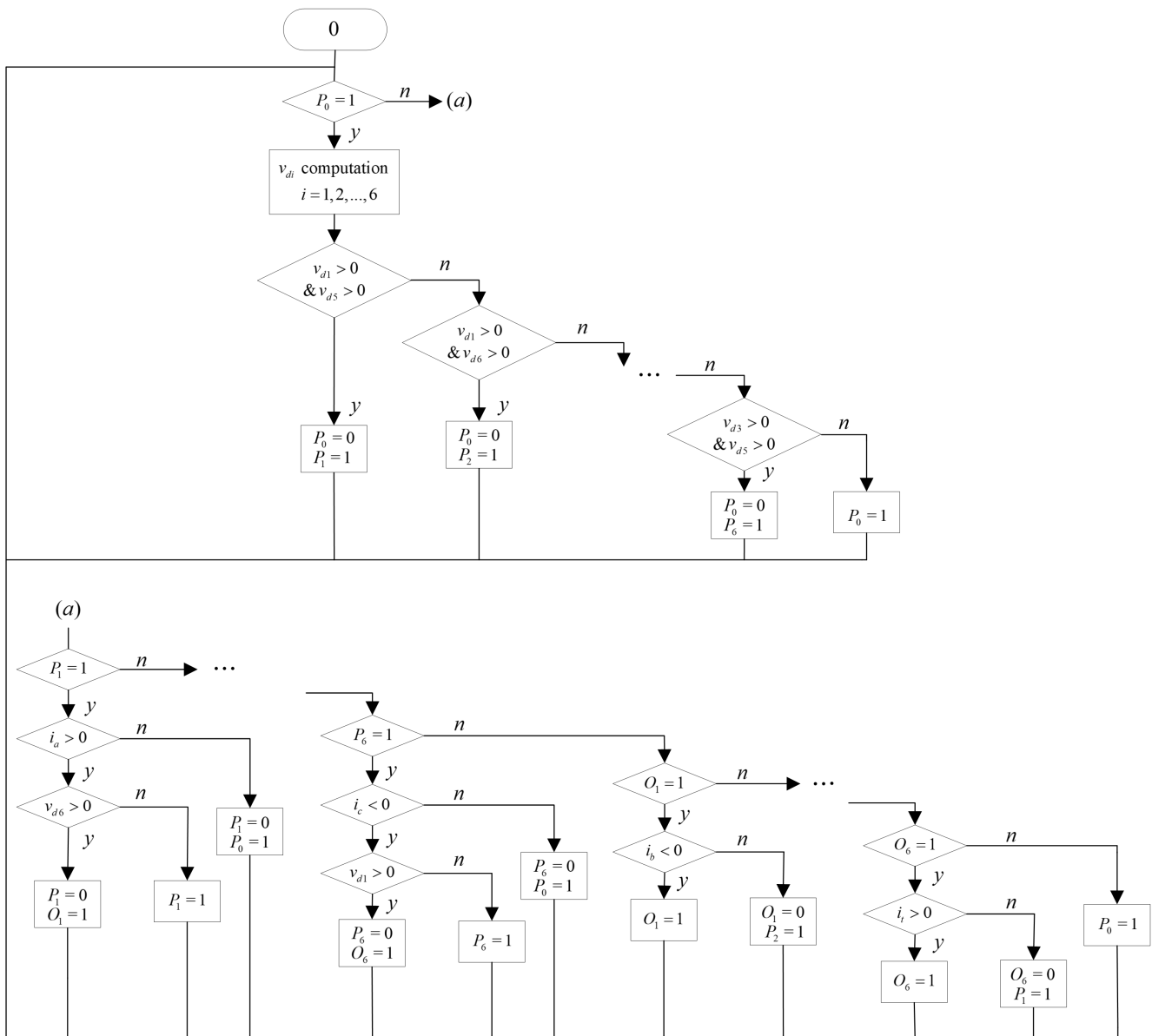


Figure 4. Flowchart of transitions between conduction and overlapping stages [34].

When the  $vd_6$  is greater than zero,  $P_1$  changes to  $O_1$ . In this regard, all three  $d_1$ ,  $d_5$ , and  $d_6$  are in on-state, resulting in the stator line voltages defined as shown in (17).

$$v_{ab} = V_O \quad v_{bc} = V_O \quad v_{ca} = 0 \tag{17}$$

Accordingly, it is possible to determine the stator line voltages in all  $P_i$  and  $O_j$  with expressions (18)–(27).

$P_2$  :

$$v_{ab} = e'_{ab} + \frac{1}{2}(e'_{ca} + V_O) \quad v_{bc} = e'_{bc} + \frac{1}{2}(e'_{ca} + V_O) \quad v_{ca} = -V_O \quad v_{d2} = \frac{1}{2}(e'_{ac} - V_O) - e'_{ab} \tag{18}$$

$O_2$  :

$$v_{ab} = 0 \quad v_{bc} = V_O \quad v_{ca} = -V_O \tag{19}$$

$P_3$  :

$$v_{ab} = e'_{ab} + \frac{1}{2}(e'_{bc} - V_O) \quad v_{bc} = V_O \quad v_{ca} = e'_{ca} + \frac{1}{2}(e'_{bc} - V_O) \quad v_{d4} = \frac{1}{2}(e'_{bc} - V_O) + e'_{ca} \tag{20}$$

$O_3 :$

$$v_{ab} = -V_O \quad v_{bc} = V_O \quad v_{ca} = 0 \tag{21}$$

$P_4 :$

$$v_{ab} = -V_O \quad v_{bc} = e'_{bc} + \frac{1}{2}(e'_{ab} + V_O) \quad v_{ca} = e'_{ca} + \frac{1}{2}(e'_{ab} + V_O) \quad v_{d3} = \frac{1}{2}(e'_{ba} - V_O) - e'_{bc} \tag{22}$$

$O_4 :$

$$v_{ab} = -V_O \quad v_{bc} = V_O \quad v_{ca} = 0 \tag{23}$$

$P_5 :$

$$v_{ab} = e'_{ab} + \frac{1}{2}(e'_{ca} - V_O) \quad v_{bc} = e'_{bc} + \frac{1}{2}(e'_{ca} - V_O) \quad v_{ca} = -V_O \quad v_{d5} = \frac{1}{2}(e'_{ca} - V_O) + e'_{ab} \tag{24}$$

$O_5 :$

$$v_{ab} = 0 \quad v_{bc} = -V_O \quad v_{ca} = V_O \tag{25}$$

$P_6 :$

$$v_{ab} = e'_{ab} + \frac{1}{2}(e'_{bc} + V_O) \quad v_{bc} = -V_O \quad v_{ca} = e'_{ca} + \frac{1}{2}(e'_{bc} + V_O) \quad v_{d1} = \frac{1}{2}(e'_{cb} - V_O) - e'_{ca} \tag{26}$$

$O_6 :$

$$v_{ab} = 0 \quad v_{bc} = -V_O \quad v_{ca} = V_O \tag{27}$$

### 2.4. MPPT Technique

Modern variable-speed WECSs benefit from several control levels that provide superior dynamic and steady-state, increase the energy conversion efficiency, reduce energy cost, and increase the lifespan of components [2]. For instance, the pitch control is a part of the high-level control, whereas the peak power extraction method, so-called MPPT, is placed at the intermediate level [2,35]. Various MPPT approaches have been studied in the literature, namely the optimal tip speed ratio control, the WT power curve-based control, the optimal torque control, the power signal feedback control, the generator signal speed feedback control, and the speed sensorless control [2]. In the present work, the optimal torque  $T_T^{OPT}$  control is utilized to compute the reference current  $I_{LB}^*$  based on (28). In this technique, the wind speed sensor is replaced by the WT rotor speed sensor. The scheme of current-mode control implementation is depicted in Figure 5 [36].

$$I_{LB}^* = \frac{T_T^{OPT} \cdot \omega_T}{V_O} = \frac{K^{OPT} \cdot \omega_T^3}{V_O} \tag{28}$$

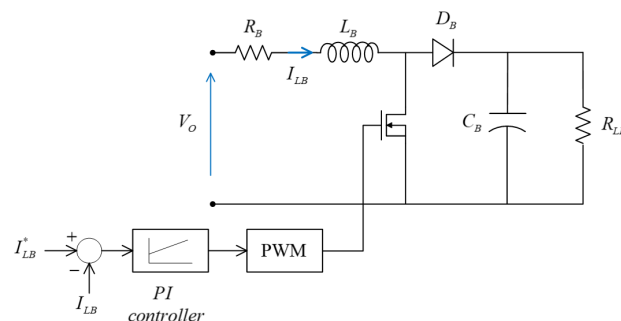
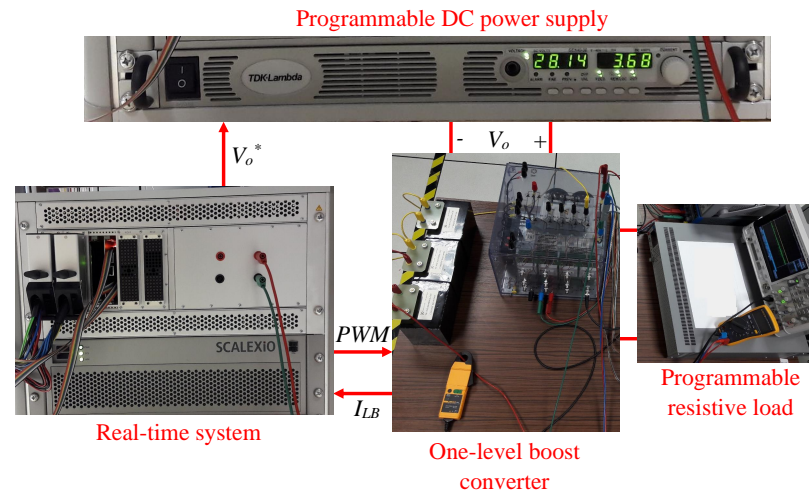


Figure 5. Scheme of one-level boost converter current-mode control.

### 3. Experimental Results

A simple standalone configuration, in which the PMSG-based WT supplies a resistive load, is studied in this article (Figure 1). Models of rotor blades, PMSG in the stationary  $abc$  reference frame, and a three-phase diode rectifier following the sequence of stages shown in Figure 3 and the flowchart shown in Figure 4 are implemented in the real-

time platform by using 12 kW direct-drive PMSG-based WECS parameters, as listed in Table 1 [31]. The inertia of rotor blades is included in  $J_t$  to achieve realistic results. The voltage, generated by the three-phase diode rectifier model, is applied on the programmable DC power supply, which is connected to a one-level hardware boost converter, as illustrated in Figure 6, when the latter supplies a resistive load of 25  $\Omega$ . In the real-time system, a target PC, having an Intel CPU E4-1275 V3 clocked at 3.8 GHz, is used. The wind profile, depicted in Figure 7, is applied to evaluate the developed real-time model performance that operates on a dSPACE real-time platform at the fixed-step sampling time of  $T_{sim} = 20 \mu s$ . The trapezoidal technique is employed for all mathematical integrations to guarantee the stability of the model [37]. To adjust the rated power of WT to the rated power of the one-level boost converter utilized in the experiments, a scaling factor of 10 is applied on the current  $I_{LB}$  and the voltage  $V_O$ . The parameters of the one-level boost converter are  $L_B = 12 \text{ mH}$ ,  $R_B = 0.9 \Omega$ , and  $C_B = 1100 \mu\text{F}$  (Figure 5). There are several approaches that can be employed to design the PI controller parameters of the one-level boost converter. They improve the control performance and ensure the stability of a PMSG-based WT. In [38,39], the process of adjusting the PI controller parameters is carried out by using particle swarm optimization (PSO) and genetic algorithm (GA) with more emphasis on control performance. In this article, these parameters are designed by using empirical Zigler–Nichols tuning method, as is proposed in [40], to ensure the stability and to achieve an acceptable dynamic performance. The same PI controller parameters are used in both DoS and DRTS cases. To illustrate the efficacy of the proposed modeling, DRTS results are compared with those obtained by DoS, which relies on the components of Matlab/Simulink Simscape toolbox, in both healthy and stator windings asymmetry fault conditions (Figure 8). The variable-step ode23 solver is selected in DoS to confirm the accuracy of numerical simulations.



**Figure 6.** Scheme of P–H–i–L system: Real–time system is connected to the programmable DC power supply, and the one–level boost converter is connected to the programmable resistive load.

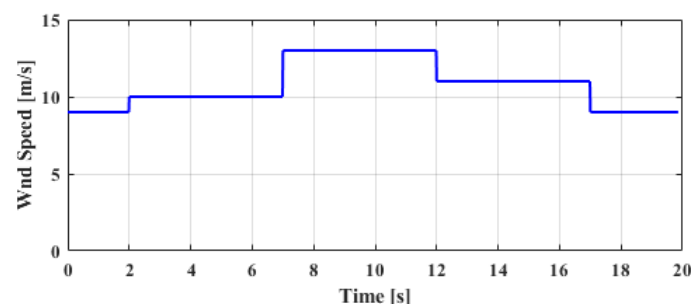


**Figure 7.** Wind speed profile.

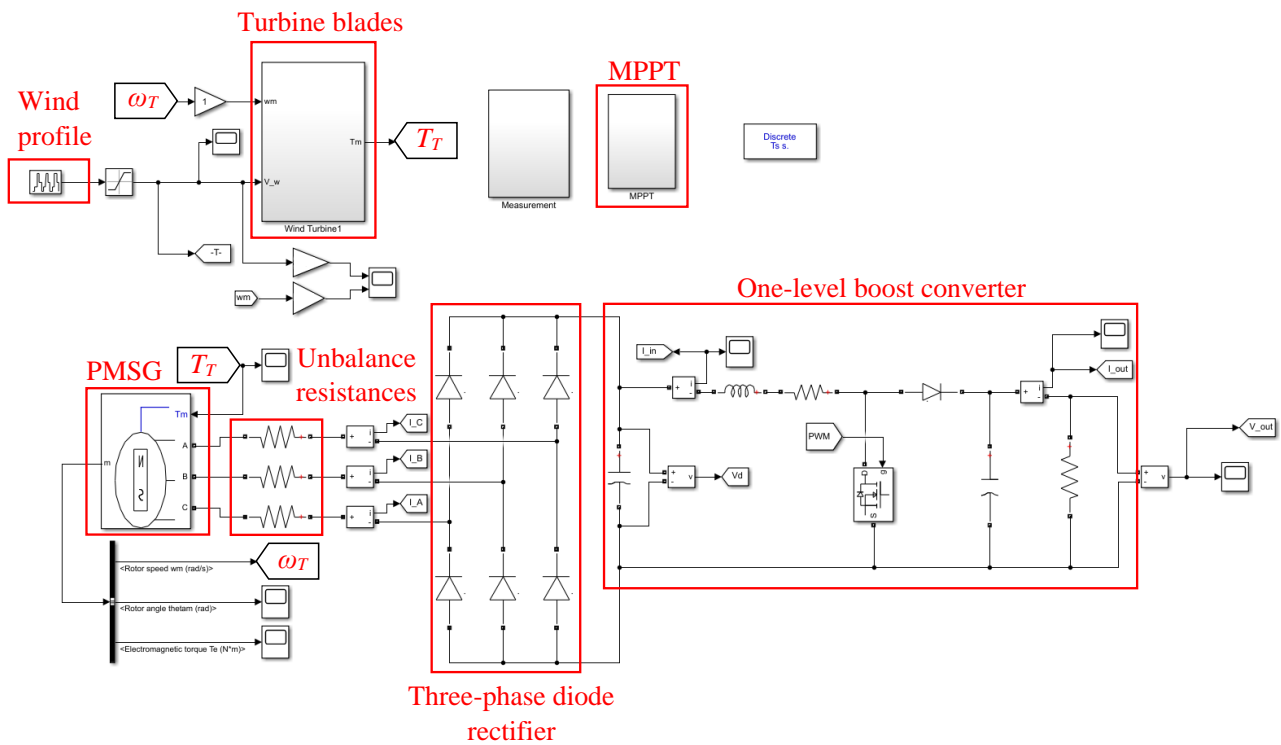


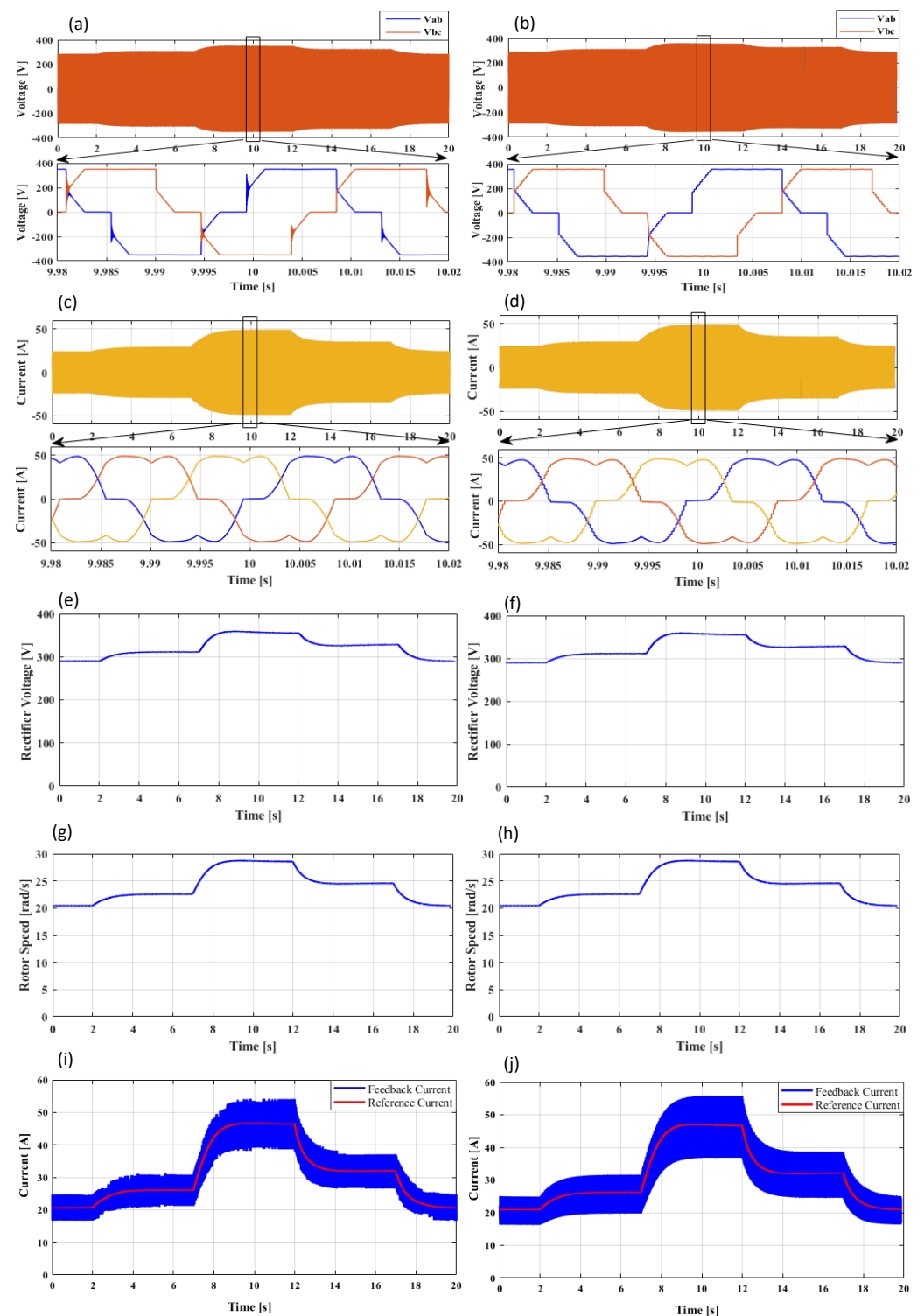
Figure 8. Model of direct-drive PMSG-based WT in Matlab/Simulink software.

Table 1. Electrical and mechanical parameters of 12 kW direct-drive PMSG-based WT.

Parameter	Value
$r_a, r_b, r_c$	1.2 $\Omega$
$L_l$	225 $\mu\text{H}$
$L_m$	2.25 mH
$J_t$	38.32 $\text{Kg}\cdot\text{m}^2$
$\psi_r$	1.28 Wb
$P_p$	8
$r_T$	3.7 m
$\lambda_{max}$	7.2
$C_{Tmax}$	0.048
$K_T$	0.002254

### 3.1. Healthy Condition

The healthy condition is studied by utilizing symmetrical stator resistances  $r_a = r_b = r_c = 1.2 \Omega$  in DRTS. Unbalance resistances, diodes' resistances in on-state, and the snubber RC circuit of all diodes are defined as  $R_{unb} = 0 \Omega$ ,  $R_{ON} = 0.01 \Omega$ ,  $R_{snubber} = 10 \text{K}\Omega$ , and  $C_{snubber} = 250 \text{nF}$ , respectively in DoS. Figure 9 illustrates the waveforms of three-phase stator line voltages ( $v_{ab}$ ,  $v_{bc}$  and  $v_{ca}$ ), three-phase stator currents ( $i_a$ ,  $i_b$  and  $i_c$ ), the three-phase diode rectifier output voltage ( $V_O$ ), the turbine rotor speed ( $\omega_T$ ), as well as reference and feedback currents at the input of the one-level boost converter for both RTDS and DoS in the time domain. Despite the usage of an ideal model for all diodes in DRTS, the results are closely matched with those obtained by DoS. The same variables are also studied in the frequency domain at the wind speed  $v_w = 10 \text{ m/s}$  in the (0 Hz, 500 Hz) frequency bandwidth by excluding the average values from all variables (Figure 10). In these previous spectra, the main frequency component corresponds to  $6 \cdot f_s$ , where  $f_s$  is the main frequency component of the stator current. It can be determined by  $f_s = P_p \cdot f_T$  ( $f_T = \frac{\omega_T}{2\pi}$ ). A close similarity is also observed between DRTS and DoS spectra.



**Figure 9.** Healthy condition DoS results in time domain. (a) Three-phase line voltages of PMSG. (c) Three-phase stator currents of PMSG. (e) Output voltage of the three-phase diode rectifier. (g) Rotor speed of PMSG. (i) Feedback and reference currents at the input of boost converter. Healthy condition DRTS results in time domain. (b) Three-phase line voltages of PMSG. (d) Three-phase stator currents of PMSG. (f) Output voltage of the three-phase diode rectifier. (h) Rotor speed of PMSG. (j) Feedback and reference currents at the input of boost converter.

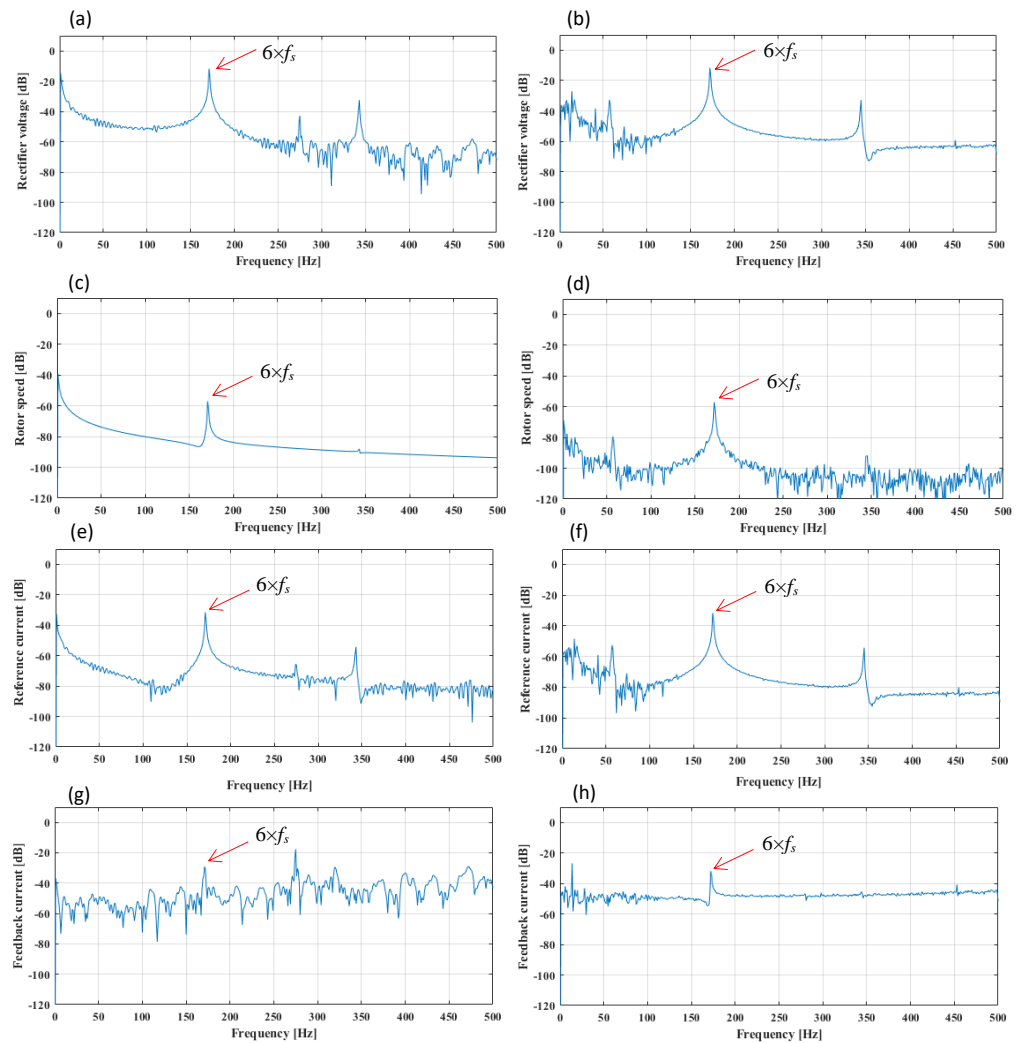


**Figure 10.** Healthy condition DoS results in frequency domain at the wind speed  $v_w = 10$  m/s. (a) Three-phase line voltages of PMSG. (c) Three-phase stator currents of PMSG. (e) Output voltage of the three-phase diode rectifier. (g) Rotor speed of PMSG. (i) Feedback and reference currents at the input of boost converter. Healthy condition DRTS results in frequency domain at the wind speed  $v_w = 10$  m/s. (b) Three-phase line voltages of PMSG. (d) Three-phase stator currents of PMSG. (f) Output voltage of the three-phase diode rectifier. (h) Rotor speed of PMSG. (j) Feedback and reference currents at the input of boost converter.

### 3.2. Stator Windings Asymmetry Fault Condition

To study the faulty condition, the stator resistance of phase  $a$  ( $r_a$ ) is increased to  $2.2 \Omega$  in DRTS. An unbalance resistance ( $R_{unb} = 1 \Omega$ ) is defined explicitly for the stator phase  $a$  in DoS. Figure 11 illustrates the waveforms of the same variables, previously studied in the healthy condition, for both RTDS and DoS in the time domain. In this case, the fault introduces negative sequence currents in the three-phase stator windings, which can be written as

$$I_a^- = I_f \sin(P_p \theta_T + \varphi_s^-) \quad I_b^- = I_f \sin(P_p \theta_T + \frac{2\pi}{3} + \varphi_s^-) \quad I_c^- = I_f \sin(P_p \theta_T - \frac{2\pi}{3} + \varphi_s^-) \quad (29)$$

The substitution of (29) into (14) yields

$$T_e^- = P_p \cdot \psi_r \times \left[ \sin(P_p \theta_T) \cdot i_a^- + \sin(P_p \theta_T - \frac{2\pi}{3}) \cdot i_b^- + \sin(P_p \theta_T + \frac{2\pi}{3}) \cdot i_c^- \right] \quad (30)$$

which gives

$$T_e^- = -\frac{3}{2} \cdot P_p \cdot \psi_r \cdot I_f \cdot \sin(2P_p\theta_T + \varphi_s^-) \quad (31)$$

In healthy PMSG, the stator currents are symmetrical, whereas in faulty PMSG, the negative sequence currents (29) appear due to the asymmetry in the stator windings. This negative sequence introduces the extra frequency component at  $2 \cdot f_s$  in the electromagnetic torque and hence in the rotor speed based on (31) and (15). Similarly, the fault-related frequency at  $2 \cdot f_s$  can introduce a new frequency component at  $4 \cdot f_s$ . This is particularly due to the electromotive force induced in the stator windings at the frequency of  $2 \cdot f_s$ . It results in new negative sequence stator currents, and hence,  $4 \cdot f_s$  appears in the electromagnetic torque. Therefore, fault-related frequency components can be formulated as  $2 \cdot k \cdot f_s$  with  $k = 1, 2, 3, \dots$ . It is worth mentioning that the amplitudes of higher-order harmonics ( $k > 1$ ), related to the fault, decrease due to the effect of system inertia. In this regard, the same variables, previously studied in the healthy condition, are analyzed in the frequency domain at the wind speed  $v_w = 10$  m/s in (0 Hz, 500 Hz) frequency bandwidth (Figure 12). As it can be expected, the fault clearly gives rise to the amplitudes of both  $2 \cdot f_s$  and  $4 \cdot f_s$  frequency components in the respective spectra.

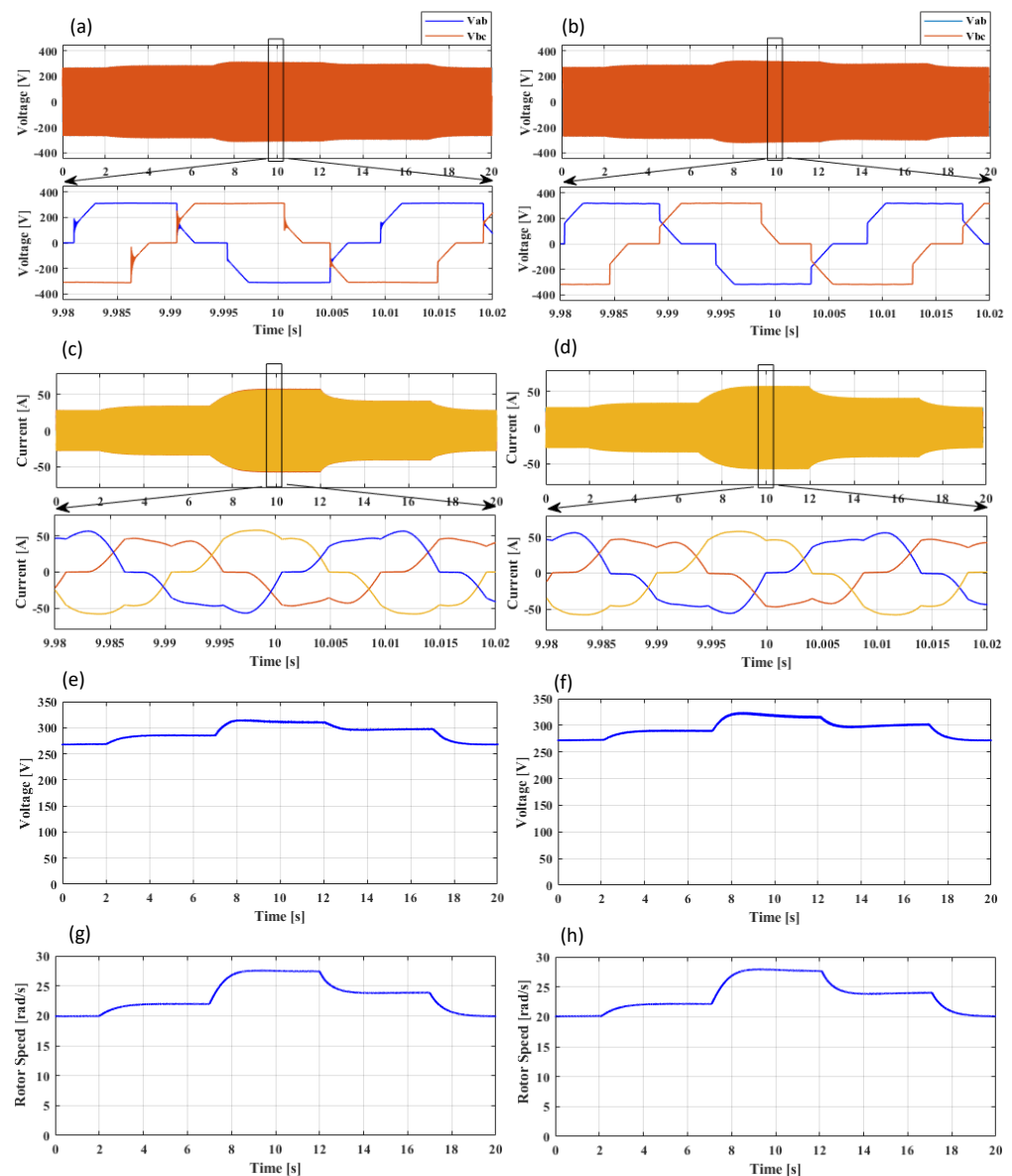
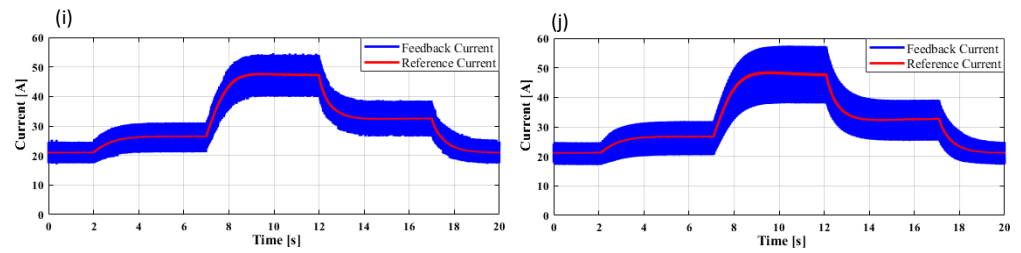
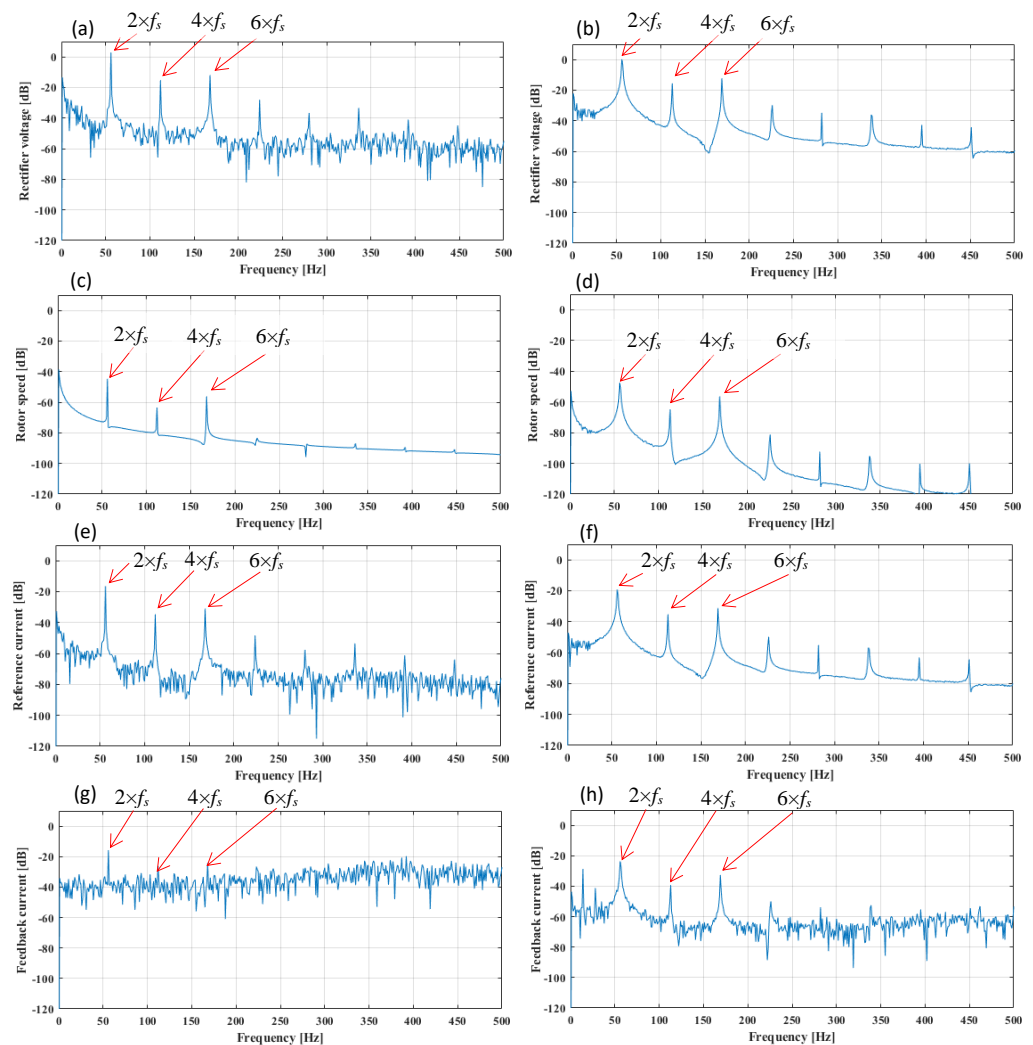


Figure 11. Cont.



**Figure 11.** Faulty condition DoS results in time domain. (a) Three-phase line voltages of PMSG. (c) Three-phase stator currents of PMSG. (e) Output voltage of the three-phase diode rectifier. (g) Rotor speed of PMSG. (i) Feedback and reference currents at the input of boost converter. Faulty condition DRTS results. (b) Three-phase line voltages of PMSG. (d) Three-phase stator currents of PMSG. (f) Output voltage of the three-phase diode rectifier. (h) Rotor speed of PMSG. (j) Feedback and reference currents at the input of boost converter.



**Figure 12.** Faulty condition DoS results in frequency domain at the wind speed  $v_w = 10$  m/s. (a) Three-phase line voltages of PMSG. (c) Three-phase stator currents of PMSG. (e) Output voltage of the three-phase diode rectifier. (g) Rotor speed of PMSG. (i) Feedback and reference currents at the input of boost converter. Faulty condition DRTS results in frequency domain at the wind speed  $v_w = 10$  m/s. (b) Three-phase line voltages of PMSG. (d) Three-phase stator currents of PMSG. (f) Output voltage of the three-phase diode rectifier. (h) Rotor speed of PMSG. (j) Feedback and reference currents at the input of boost converter.

#### 4. Conclusions

In this article, a P-H-i-L framework is proposed for studying the stator windings asymmetry fault in direct-drive PMSG-based WTs, having passive converters at the generator side. Such a configuration is particularly interesting, since it allows the real-time evaluation of newly developed fault-tolerant control and condition monitoring techniques at a lower cost and in a realistic way. In addition, it avoids the field test on a full-scale WECS, which is commonly a complex task in practice. Furthermore, this reconfigurable simulation environment enables the study of a wide range of electrical and mechanical faults that may take place in the drive-train. For instance, the stator windings asymmetry fault is identified by using the spectrum analysis of the variables such as rotor speed, three-phase diode rectifier output voltage as well as feedback and reference currents at the input of a one-level boost converter. In this regard, the mathematical models of turbine blades, PMSG in the *abc* reference frame, and the three-phase diode rectifier are all implemented in a real-time system. The voltage, generated by the three-phase diode rectifier model, is connected to a one-level hardware boost converter through a commercial programmable DC power supply. It is observed that the fault clearly gives rise to the amplitudes of  $2 \cdot k \cdot f_s$  frequency components, where  $k$  is an integer, particularly  $2 \cdot f_s$  and  $4 \cdot f_s$  in the studied signatures. DRTS results are compared with DoS results, which relied on a Matlab/Simulink Simscape model to demonstrate the efficacy of the proposed framework.

**Author Contributions:** Conceptualization, M.Y., S.H.K. and M.H.M.; methodology, M.Y., S.H.K. and M.H.M.; software, M.Y., S.H.K. and M.H.M.; validation, M.Y., S.H.K. and M.H.M.; formal analysis, M.Y., S.H.K., M.H.M., D.A.K. and H.R.; investigation, M.Y., S.H.K. and M.H.M.; resources, M.Y., S.H.K.; data curation, M.Y. and S.H.K.; writing—original draft preparation, M.Y., S.H.K., M.H.M., D.A.K. and H.R.; writing—review and editing, M.Y., S.H.K., M.H.M., D.A.K. and H.R.; visualization, M.Y., S.H.K., M.H.M., D.A.K. and H.R.; supervision, S.H.K.; project administration, S.H.K.; funding acquisition, S.H.K. All authors have read and agreed to the published version of the manuscript.

**Funding:** This research received no external funding.

**Data Availability Statement:** Not applicable.

**Conflicts of Interest:** The authors declare no conflict of interest.

#### Abbreviations

The following abbreviations used in this manuscript:

FPGA	Field-Programmable Gate Arrays
DRTS	Digital Real-Time Simulation
DoS	Digital offline Simulation
RTDS	Real-Time Digital Simulator
PMSG	Permanent Magnet Synchronous Generator
WT	Wind Turbine
TSR	Tip-Speed Ratio
MPPT	Maximum Power Point Tracking
P-H-i-L	Power-Hardware-in-the-Loop
H-i-L	Hardware-in-the-Loop
P-i-L	Processor-in-the-Loop
S-i-L	Software-in-the-Loop
WECS	Wind Energy Conversion System
$\rho$	Air density ( $\text{kg/m}^3$ )
$r_T$	Blade radius (m)
$v_w$	Wind speed (m/s)
$\lambda$	TSR
$\omega_T$	Turbine rotor speed (rad/s)
$v_a, v_b, v_c$	PMSG phase <i>abc</i> stator voltages (V)
$i_a, i_b, i_c$	PMSG <i>abc</i> stator currents (A)
$\phi_a, \phi_b, \phi_c$	PMSG <i>abc</i> stator flux linkages (Wb)

$e_a, e_b, e_c$	Stator electromotive forces (V)
$r_a, r_b, r_c$	Stator windings resistances ( $\Omega$ )
$I_f$	Amplitude of negative sequence currents (A)
$I_{LB}$	Current at the input of one-level boost converter (A)
$I_{LB}^*$	Reference current at the input of one-level boost converter (A)
$\varphi_s^-$	Phase of negative sequence currents (rad)
$\psi_r$	Flux linkage peak value of permanent magnets (Wb)
$\theta_T$	Turbine rotor position angle (rad)
$P_p$	Number of pole pairs in PMSG
$L_m$	Magnetization inductance (H)
$L_l$	Leakage inductance (H)
$J_t$	Total moment of inertia ( $\text{Kg.m}^2$ )
$B_t$	Viscous friction (N.m.s)

## References

1. Qiao, W.; Lu, D. A Survey on Wind Turbine Condition Monitoring and Fault Diagnosis—Part I: Components and Subsystems. *IEEE Trans. Ind. Electron.* **2015**, *62*, 6536–6545. [\[CrossRef\]](#)
2. Yaramasu, V.; Wu, B. Basics of Wind Energy Conversion Systems (WECS). In *Model Predictive Control of Wind Energy Conversion Systems*; John Wiley & Sons: Hoboken, NJ, USA, 2017; pp. 1–60. [\[CrossRef\]](#)
3. Gao, Z.; Sheng, S. Real-time Monitoring, Prognosis, and Resilient Control for Wind Turbine Systems. *Renew. Energy* **2018**, *116*, 1–4. [\[CrossRef\]](#)
4. Gao, Z.; Liu, X. An Overview on Fault Diagnosis, Prognosis and Resilient Control for Wind Turbine Systems. *Processes* **2021**, *9*, 300. [\[CrossRef\]](#)
5. Kia, S.H.; Henaou, H.; Capolino, G.A.; Marzabali, M.H. A Reduced-Scale Test Bench Dedicated to Electrical and Mechanical Faults Studies in Wind Turbine Generators. In Proceedings of the 2018 IEEE International Conference on Industrial Technology (ICIT), Lyon, France, 20–22 February 2018; pp. 2021–2027. [\[CrossRef\]](#)
6. Lentijo, S.; D’Arco, S.; Monti, A. Comparing the Dynamic Performances of Power Hardware-in-the-Loop Interfaces. *IEEE Trans. Ind. Electron.* **2010**, *57*, 1195–1207. [\[CrossRef\]](#)
7. Yousefzadeh, M.; Kia, S.H.; Arab Khaburi, D. Emulation of Direct-Drive Wind Energy Conversion Systems Based on Permanent Magnet Synchronous Generators. In Proceedings of the 2021 12th Power Electronics, Drive Systems, and Technologies Conference (PEDSTC), Tabriz, Iran, 2–4 February 2021; pp. 1–5. [\[CrossRef\]](#)
8. Kuffel, R.; Giesbrecht, J.; Maguire, T.; Wierckx, R.; McLaren, P. RTDS—a Fully Digital Power System Simulator Operating in Real Time. In Proceedings of the IEEE WESCANEX 95. Communications, Power, and Computing. Conference Proceedings, Winnipeg, MB, Canada, 15–16 May 1995; Volume 2, pp. 300–305. [\[CrossRef\]](#)
9. Abourida, S.; Dufour, C.; Belanger, J.; Murere, G.; Lechevin, N.; Yu, B. Real-Time PC-based Simulator of Electric Systems and Drives. In Proceedings of the Seventeenth Annual IEEE Applied Power Electronics Conference and Exposition (Cat. No.02CH37335), Dallas, TX, USA, 10–14 March 2002; Volume 1, pp. 433–438. [\[CrossRef\]](#)
10. Mirz, M.; Dinkelbach, J.; Monti, A. DPsim—Advancements in Power Electronics Modelling Using Shifted Frequency Analysis and in Real-Time Simulation Capability by Parallelization. *Energies* **2020**, *13*, 3879. [\[CrossRef\]](#)
11. Estrada, L.; Vazquez, N.; Vaquero, J.; de Castro, A.; Arau, J. Real-Time Hardware in the Loop Simulation Methodology for Power Converters Using LabVIEW FPGA. *Energies* **2020**, *13*, 373. [\[CrossRef\]](#)
12. Omar Faruque, M.D.; Strasser, T.; Lauss, G.; Jalili-Marandi, V.; Forsyth, P.; Dufour, C.; Dinavahi, V.; Monti, A.; Kotsampopoulos, P.; Martinez, J.A.; et al. Real-Time Simulation Technologies for Power Systems Design, Testing, and Analysis. *IEEE Power Energy Technol. Syst. J.* **2015**, *2*, 63–73. [\[CrossRef\]](#)
13. Bai, H.; Liu, C.; Breaz, E.; Al-Haddad, K.; Gao, F. A Review on the Device-Level Real-Time Simulation of Power Electronic Converters: Motivations for Improving Performance. *IEEE Ind. Electron. Mag.* **2021**, *15*, 12–27. [\[CrossRef\]](#)
14. Nzale, W.; Mahseredjian, J.; Fu, X.; Kocar, I.; Dufour, C. Improving Numerical Accuracy in Time-Domain Simulation for Power Electronics Circuits. *IEEE Open Access J. Power Energy* **2021**, *8*, 157–165. [\[CrossRef\]](#)
15. Bouscayrol, A. Different Types of Hardware-In-the-Loop Simulation for Electric Drives. In Proceedings of the 2008 IEEE International Symposium on Industrial Electronics, Cambridge, UK, 30 June–2 July 2008; pp. 2146–2151. [\[CrossRef\]](#)
16. Guo, B.; Mohamed, A.; Bacha, S.; Alamir, M.; Boudinet, C.; Pouget, J. Reduced-Scale Models of Variable Speed Hydro-Electric Plants for Power Hardware-in-the-Loop Real-Time Simulations. *Energies* **2020**, *13*, 5764. [\[CrossRef\]](#)
17. Song, J.; Hur, K.; Lee, J.; Lee, H.; Lee, J.; Jung, S.; Shin, J.; Kim, H. Hardware-in-the-Loop Simulation Using Real-Time Hybrid-Simulator for Dynamic Performance Test of Power Electronics Equipment in Large Power System. *Energies* **2020**, *13*, 3955. [\[CrossRef\]](#)
18. Barragán-Villarejo, M.; García-López, F.d.P.; Marano-Marcolini, A.; Maza-Ortega, J.M. Power System Hardware in the Loop (PSHIL): A Holistic Testing Approach for Smart Grid Technologies. *Energies* **2020**, *13*, 3858. [\[CrossRef\]](#)
19. Vogel, S.; Nguyen, H.T.; Stevic, M.; Jensen, T.V.; Heussen, K.; Rajkumar, V.S.; Monti, A. Distributed Power Hardware-in-the-Loop Testing Using a Grid-Forming Converter as Power Interface. *Energies* **2020**, *13*, 3770. [\[CrossRef\]](#)

20. Helmedag, A.; Isermann, T.; Monti, A. Fault Ride Through Certification of Wind Turbines Based on a Power Hardware in the Loop Setup. In Proceedings of the 2013 IEEE International Workshop on Applied Measurements for Power Systems (AMPS), Aachen, Germany, 25–27 September 2013; pp. 150–155. [\[CrossRef\]](#)
21. Helmedag, A.; Isermann, T.; Monti, A.; Averous, N.R.; Stieneker, M.; De Doncker, R.W. Multi-Physics Power Hardware in the Loop Test Bench for On-shore Wind Turbine Nacelles. In Proceedings of the 2013 IEEE ECCE Asia Downunder, Melbourne, Australia, 3–6 June 2013; pp. 221–226. [\[CrossRef\]](#)
22. Neshati, M.; Zuga, A.; Jersch, T.; Wenske, J. Hardware-in-the-loop Drive Train Control for Realistic Emulation of Rotor Torque in a Full-scale Wind Turbine Nacelle Test rig. In Proceedings of the European Control Conference (ECC'2016), Aalborg, Denmark, 29 June–1 July 2016; pp. 1481–1486. [\[CrossRef\]](#)
23. Zhang, Z.; Wang, F.; Acikgoz, M.; Cai, X.; Kennel, R. FPGA HiL simulation of Back-to-Back Converter PMSG Wind Turbine Systems. In Proceedings of the 2015 9th International Conference on Power Electronics and ECCE Asia (ICPE-ECCE Asia), Seoul, Korea, 1–5 June 2015; pp. 99–106. [\[CrossRef\]](#)
24. Dufour, C.; Belanger, J. A Real-Time Simulator for Doubly fed Induction Generator Based Wind Turbine Applications. In Proceedings of the 2004 IEEE 35th Annual Power Electronics Specialists Conference (IEEE Cat. No.04CH37551), Aachen, Germany, 20–25 June 2004; Volume 5, pp. 3597–3603. [\[CrossRef\]](#)
25. Terron-Santiago, C.; Martinez-Roman, J.; Puche-Panadero, R.; Sapena-Bano, A. Low-Computational-Cost Hybrid FEM-Analytical Induction Machine Model for the Diagnosis of Rotor Eccentricity, Based on Sparse Identification Techniques and Trigonometric Interpolation. *Sensors* **2021**, *21*, 6963. [\[CrossRef\]](#) [\[PubMed\]](#)
26. Sapena-Bano, A.; Riera-Guasp, M.; Martinez-Roman, J.; Pineda-Sanchez, M.; Puche-Panadero, R.; Perez-Cruz, J. FEM-Analytical Hybrid Model for Real Time Simulation of IMs Under Static Eccentricity Fault. In Proceedings of the 2019 IEEE 12th International Symposium on Diagnostics for Electrical Machines, Power Electronics and Drives (SDEMPED), Toulouse, France, 27–30 August 2019; pp. 108–114. [\[CrossRef\]](#)
27. Kia, S.H. Detection of Stator and Rotor Asymmetries Faults in Wound Rotor Induction Machines: Modeling, Test and Real-Time Implementation. In *Emerging Electric Machines*; Zobia, A.F., Aleem, S.H.A., Eds.; IntechOpen: Rijeka, Croatia, 2021; Chapter 3. [\[CrossRef\]](#)
28. Xu, S.; Tao, S.; Zheng, W.; Chai, Y.; Ma, M.; Ding, L. Multiple Open-Circuit Fault Diagnosis for Back-to-Back Converter of PMSG Wind Generation System Based on Instantaneous Amplitude Estimation. *IEEE Trans. Instrum. Meas.* **2021**, *70*, 1–13. [\[CrossRef\]](#)
29. Freire, N.M.A.; Estima, J.O.; Marques Cardoso, A.J. Open-Circuit Fault Diagnosis in PMSG Drives for Wind Turbine Applications. *IEEE Trans. Ind. Electron.* **2013**, *60*, 3957–3967. [\[CrossRef\]](#)
30. Kia, S.H.; Henao, H.; Capolino, G.A.; Marzabali, M.H. Contribution to Wind Turbine Emulation Based on Wound Rotor Induction Machine Configuration. In Proceedings of the 2018 IEEE International Conference on Industrial Technology (ICIT), Lyon, France, 19–22 February 2018; pp. 2028–2034. [\[CrossRef\]](#)
31. Chen, J.; Chen, J.; Gong, C. On Optimizing the Aerodynamic Load Acting on the Turbine Shaft of PMSG-Based Direct-Drive Wind Energy Conversion System. *IEEE Trans. Ind. Electron.* **2014**, *61*, 4022–4031. [\[CrossRef\]](#)
32. Abdullah, M.; Yatim, A.; Tan, C.; Saidur, R. A Review of Maximum Power Point Tracking Algorithms for Wind Energy Systems. *Renew. Sustain. Energy Rev.* **2012**, *16*, 3220–3227. [\[CrossRef\]](#)
33. Pillay, P.; Krishnan, R. Modeling of Permanent Magnet Motor Drives. *IEEE Trans. Ind. Electron.* **1988**, *35*, 537–541. [\[CrossRef\]](#)
34. Batard, C.; Poitiers, F.; Machmoum, M. An Original Method to Simulate Diodes Rectifiers Behaviour with Matlab-Simulink Taking into Account Overlap Phenomenon. In Proceedings of the 2007 IEEE International Symposium on Industrial Electronics, Vigo, Spain, 4–7 June 2007; pp. 971–976. [\[CrossRef\]](#)
35. Gao, R.; Gao, Z. Pitch Control for Wind Turbine Systems Using Optimization, Estimation and Compensation. *Renew. Energy* **2016**, *91*, 501–515. [\[CrossRef\]](#)
36. Yousefzadeh, M.; Kia, S.H.; Arab Khaburi, D.; El Hajjaji, A. Boost-in-the-Loop for Real-Time Evaluation of Wind Turbines Based on PMSG. In Proceedings of the 2021 23rd European Conference on Power Electronics and Applications (EPE'21 ECCE Europe), Ghent, Belgium, 6–10 September 2021; pp. 1–8.
37. Ametani, A. *Numerical Analysis of Power System Transients and Dynamics*; Energy Engineering, Institution of Engineering and Technology: Stevenage, UK, 2015.
38. Kim, Y.S.; Chung, I.Y.; Moon, S.I. Tuning of the PI Controller Parameters of a PMSG Wind Turbine to Improve Control Performance under Various Wind Speeds. *Energies* **2015**, *8*, 1406–1425 [\[CrossRef\]](#)
39. Hasanien, H.M.; Muyeen, S.M. Design Optimization of Controller Parameters Used in Variable Speed Wind Energy Conversion System by Genetic Algorithms. *IEEE Trans. Sustain. Energy* **2012**, *3*, 200–208. [\[CrossRef\]](#)
40. Haque, M.E.; Negnevitsky, M.; Muttaqi, K.M. A Novel Control Strategy for a Variable-Speed Wind Turbine With a Permanent-Magnet Synchronous Generator. *IEEE Trans. Ind. Appl.* **2010**, *46*, 331–339. [\[CrossRef\]](#)